Giant low-field magnetocaloric effect of (Er,Y)Cr₂Si₂ compounds at ultra-low temperatures

Lei Xi[1,2], Xinqi Zheng[1*], Yawei Gao[1], Jiawang Xu[3,4], Chaofan Liu[1], Dingsong Wang[1], Juping Xu[5,6], Wen Yin[5,6], Shuxian Yang[1,3], Baojie Jin[1], Mengyuan Zhu[1], Weifeng Xu[1], Jianxin Shen[1], Jingyan Zhang[1], He Huang[1], Yanfei Wu[1], Fei Gu[1], Huiyu Shi[1], Yixuan Tao[1], Shouguo Wang[1,2*] and Baogen Shen[3,7]

ABSTRACT Low-temperature and low-field magnetocaloric materials with high magnetocaloric effect (MCE) performance have important prospects in applications such as gas liquefaction. A series of polycrystalline $Er_{1-x}Y_xCr_2Si_2$ ($0 \leq x \leq 0.8$) samples were successfully synthesized by arc melting, showing giant low-field MCE. For the sample with $x = 0.1$, the compound shows the best MCE performance, with the appropriate working temperature down to 2 K. Furthermore, the maximum value of magnetic entropy change (($-\Delta S_M)_{max}$) and adiabatic temperature change (($\Delta T_{ad})_{max}$) under the field change of 0–1 T are calculated to be 19.2 J kg^{-1} K^{-1} and 4.3 K correspondingly. The value of $(-\Delta S_M)_{max}$ is the largest ever reported for intermetallic MCE materials below 20 K. The characteristic of magnetic phase transition is verified to be of second order on basis of Arrott plots, mean field theory and rescaled universal $-\Delta S_M$ curves. The physical mechanism indicates that the great enhancement of $(-\Delta S_M)_{max}$ as large as 15.9% due to 10% Y substitution originates from the larger saturation magnetic moments and the smaller saturated magnetic fields.

Keywords: magnetocaloric effect, magnetic structure, RCr₂Si₂ compounds

INTRODUCTION

Magnetic refrigerant materials are the core working substance of magnetic refrigeration technology, which is based on the magnetocaloric effect (MCE) and considered as a potential alternative to the traditional gas compression-expansion cooling technology due to its environmental friendliness and high energy efficiency [1–4]. Magnetic refrigerant materials working at room temperature have been investigated with persistent efforts for the application prospect in air conditioner or refrigerator, such as Gd-Si-Ge [5], La-Fe-Si [6], Ni-Mn-based Heusler alloys [7,8] and Mn-based series [9,10]. In recent years, mag-

netocaloric materials working at low temperatures have also drawn much attention for the potential application in gas liquefaction. A lot of low-temperature magnetocaloric materials with large MCE have been reported, such as ErCo₂ [11], HoB₂ [12], EuS [13], Eu₂In [14], TmCoSi [15], Er₀.₉Ho₀.₁Ni [16], ErMn₂Si₂ [17] GdFe₂Si₂ [18], ErNiGa₂ [19], Er₂Cr₂C₃ [20] and rare-earth-based perovskite oxides [21–23]. However, not only the improvement on MCE performance but also the related physical mechanism should be further clarified. Firstly, specified working temperature is of great importance to the applications of MCE materials. For example, the transition temperature of MCE materials used for hydrogen and helium liquefaction should be close to liquid hydrogen/helium temperatures. Secondly, large MCE at low fields is better for practical applications compared with high-filed MCE because the applicable magnetic field is usually less than 1.5 T for most of the reported magnetic refrigerators [24–26]. Thirdly, the physical mechanism related with the second-order phase transition is considerably important for MCE materials because good thermal and magnetic reversibility is expected in this case [27]. Therefore, it is urgent to explore MCE materials with ultra-low working temperatures, large MCE at low fields and second-order magnetic transition.

Rare-earth-based ternary RCr₂Si₂ (R = rare earth) intermetallic compounds have a ThCr₂Si₂-type tetragonal structure (space group $I/4mmm$) and the main magnetic transition temperature is about 4.5 and 3 K for GdCr₂Si₂ and TbCr₂Si₂, respectively [28–33]. The magnetic ordering of rare earth atoms was not observed at 2 K for HoCr₂Si₂, ErCr₂Si₂ and TmCr₂Si₂ compounds, indicative of the ultra-low transition temperatures [29,31,32]. The Cr atoms are antiferromagnetically ordered at 758, 718 and 692 K for TbCr₂Si₂, HoCr₂Si₂ and ErCr₂Si₂, respectively [34]. However, no high-temperature ordering of Cr moments was observed according to the heat capacity (HC), alternating current (AC) susceptibility and first-principles calculations [32]. The magnetic transition temperature of ErCr₂Si₂ is around 1.9 K, and the maximum of magnetic entropy change (($-\Delta S_M)_{max}$) and

[1] School of Materials Science and Engineering, Beijing Advanced Innovation Center for Materials Genome Engineering, University of Science and Technology Beijing, Beijing 100083, China
[2] School of Materials Science and Engineering, Anhui University, Hefei 230601, China
[3] Beijing National Laboratory for Condensed Matter Physics, Institute of Physics, Chinese Academy of Sciences & University of Chinese Academy of Sciences, Beijing 100190, China
[4] Songshan Lake Materials Laboratory, Dongguan 523808, China
[5] Institute of High Energy Physics, Chinese Academy of Sciences, Beijing 100049, China
[6] Spallation Neutron Source Science Center, Dongguan 523803, China
[7] Ningbo Institute of Materials Technology and Engineering, Chinese Academy of Sciences, Ningbo 315201, China
* Corresponding authors (emails: zhengxq@ustb.edu.cn (Zheng X); sgwang@ustb.edu.cn (Wang S))

adiabatic temperature change $((\Delta T_{ad})_{max})$ are 24.1 J kg^{-1} K^{-1} and 8.4 K, respectively, for the field change of 0–2 T [35].

In this work, a series of Er$_{1-x}$Y$_x$Cr$_2$Si$_2$ ($0 \leqslant x \leqslant 0.8$) compounds were synthesized and the influence of Y-substitution for Er atoms on the magnetic properties and MCE was investigated in detail. For $x = 0.1$, the compound Er$_{0.9}$Y$_{0.1}$Cr$_2$Si$_2$ exhibits the best MCE performance, where the maximum value of magnetic entropy change $((-\Delta S_M)_{max})$ and adiabatic temperature change $((\Delta T_{ad})_{max})$ under the field change of 0–1 T reach as high as 19.2 J kg^{-1} K^{-1} and 4.3 K, respectively. The physical mechanism about the great enhancement due to Y substitution originates from the larger saturation magnetic moments and the smaller saturated magnetic fields.

EXPERIMENTAL SECTION

Sample synthesis
Polycrystalline Er$_{1-x}$Y$_x$Cr$_2$Si$_2$ ($x = 0, 0.1, 0.2, 0.3, 0.4, 0.6$ and 0.8) were synthesized by arc melting Er, Y, Cr and Si elementary substance with the purity higher than 99.9 wt% under the argon atmosphere protection. Due to volatilization, 2% of Er and Y were over added into the stoichiometric amounts of mixture before melting. To ensure compositional homogeneity, the obtained ingots were melted four times on a water-cooled copper hearth, annealed at 1073 K for seven days in evacuated quartz tubes, and then quenched into liquid nitrogen to avoid the formation of large grain.

X-ray diffraction (XRD)
The annealed samples were ground into powder and the phase purity together with crystal structure was examined by powder XRD experiments with Cu-Kα radiation (wavelength λ = 1.5406 Å) measured at a step of 0.02 degree. The Rietveld refinement analysis was performed by using the program of GSAS [36].

Transmission electron microscopy (TEM) investigation
The high-resolution (HR) images of Er$_{0.9}$Y$_{0.1}$Cr$_2$Si$_2$ sample were obtained on a field-emission TEM (JEOL JSM-2200FS and JEOL LM-2100F) and the elemental mapping and component analysis were carried out by the energy dispersive X-ray spectroscopic (EDS) equipped with TEM. The sample was crashed into powder, scattered in alcohol by ultrasound and then dripped on the ultra-thin carbon film for TEM analysis.

Neutron powder diffraction (NPD)
NPD measurements were performed at 5 K on the Multi-Physics Instrument (MPI) at the China Spallation Neutron Source (CSNS). The samples were loaded in 9.0 mm vanadium cans and diffraction patterns were collected in the time-of-flight (T.O.F.) mode with wavelength bands of 0.1–4.5 Å. The diffraction patterns were collected by detector arrays marked as Bank-A, Bank-B and Bank-C with diffraction angle 2θ of 35°, 95° and 132°, respectively. The low temperature of 5 K was achieved with cryostat (CCR06) and the sample was kept at 5 K for 30 min before measurements. The program of GSAS was used for the Rietveld refinement of NPD patterns [37].

Magnetic properties measurements
The thermal magnetization and isothermal magnetization curves were measured on the Vibrating Sample Magnetometer with

quantum design (SQUID-VSM) and a Physical Property Measurement System (PPMS-14). The thermal magnetization measurements were carried out from 2 K and the isothermal magnetization measurements were performed by a stable mode at each point with the applied magnetic field up to 7 T. Furthermore, the oscillatory demagnetization was performed before isothermal magnetization measurements to eliminate the influence of residual magnetization possibly caused by the previous magnetizing (MH) curve measurement.

HC measurements
Specific heat measurements were carried out by using PPMS as well. The HC data were collected with temperature increasing from 2 K under the magnetic field of 0 and 0.5 T separately. In order to obtain accurate HC data, each HC curve was measured twice in the mode with sample and without sample. The final HC data were obtained by subtracting the data of sample holder together with glue from the total measured data.

RESULTS AND DISCUSSION

Crystal structure and phase analysis
The powder XRD patterns for Er$_{1-x}$Y$_x$Cr$_2$Si$_2$ ($0 \leqslant x \leqslant 0.8$) were obtained at room temperature and then fitted by the Rietveld refinement method. The XRD pattern and Rietveld refinement fitting curve of Er$_{0.9}$Y$_{0.1}$Cr$_2$Si$_2$ are presented in Fig. 1a and all the XRD patterns of Er$_{1-x}$Y$_x$Cr$_2$Si$_2$ ($0 \leqslant x \leqslant 0.8$) are shown in Fig. 1b. It is found that Er$_{0.9}$Y$_{0.1}$Cr$_2$Si$_2$ has the ThCr$_2$Si$_2$-type tetragonal structure (space group No. 139, $I4/mmm$) according to fitting results, which is in accord with the literature [35]. The detailed unit cell of Er$_{0.9}$Y$_{0.1}$Cr$_2$Si$_2$ is shown in the inset of Fig. 1a. There are two rare earth (R) atoms, four Cr atoms and four Si atoms in each unit cell, occupying 2a, 4d and 4e site correspondingly and with symmetry of $(4/mmm)$, $(-4m2)$, $(4mm)$, respectively. The lattice parameter is determined as $a = b = 3.8911(2)$ Å, $c = 10.6245(5)$ Å, and $V = 160.86(2)$ Å^3. The coordinates of Si are determined as (0, 0, 0.3861(6)) and the coordinates of R and Cr are fixed according to the requirement of symmetry. Er and Y atoms occupy the same site and the atomic ratio was set as 9:1. The standard Bragg positions of Er$_{0.9}$Y$_{0.1}$Cr$_2$Si$_2$ locate at the bottom of Fig. 1b. Almost all of the diffraction peaks on the XRD patterns of Er$_{1-x}$Y$_x$Cr$_2$Si$_2$ ($0 \leqslant x \leqslant 0.8$) can be indexed to the positions and no extra peaks are observed, indicating that Er$_{1-x}$Y$_x$Cr$_2$Si$_2$ ($0 \leqslant x \leqslant 0.8$) are all pure phases and isostructural samples. In addition, it can be seen that the diffraction peaks move towards lower 2θ with increasing Y-content. Actually, all the XRD patterns of Er$_{1-x}$Y$_x$Cr$_2$Si$_2$ ($0 \leqslant x \leqslant 0.8$) are fitted and the Y-content dependences of lattice parameters are presented in Fig. 1c. It is found that all the lattice parameters show a monotonously increase by linear relationship with the content of Y. On the one hand, it further indicates that Er$_{1-x}$Y$_x$Cr$_2$Si$_2$ ($0 \leqslant x \leqslant 0.8$) have the same structure and Y-substitution for Er atoms only makes changes on the size of unit cell rather than the symmetry of structure. On the other hand, it confirms that Y-substitution enlarges the unit cell, which is in keeping with the phenomenon that diffraction peak slightly moves towards lower 2θ with increasing content of Y as shown in Fig. 1b. That is because there is a negative relationship between interplanar spacing and diffraction angle according to Bragg equation as described in Equation (1).
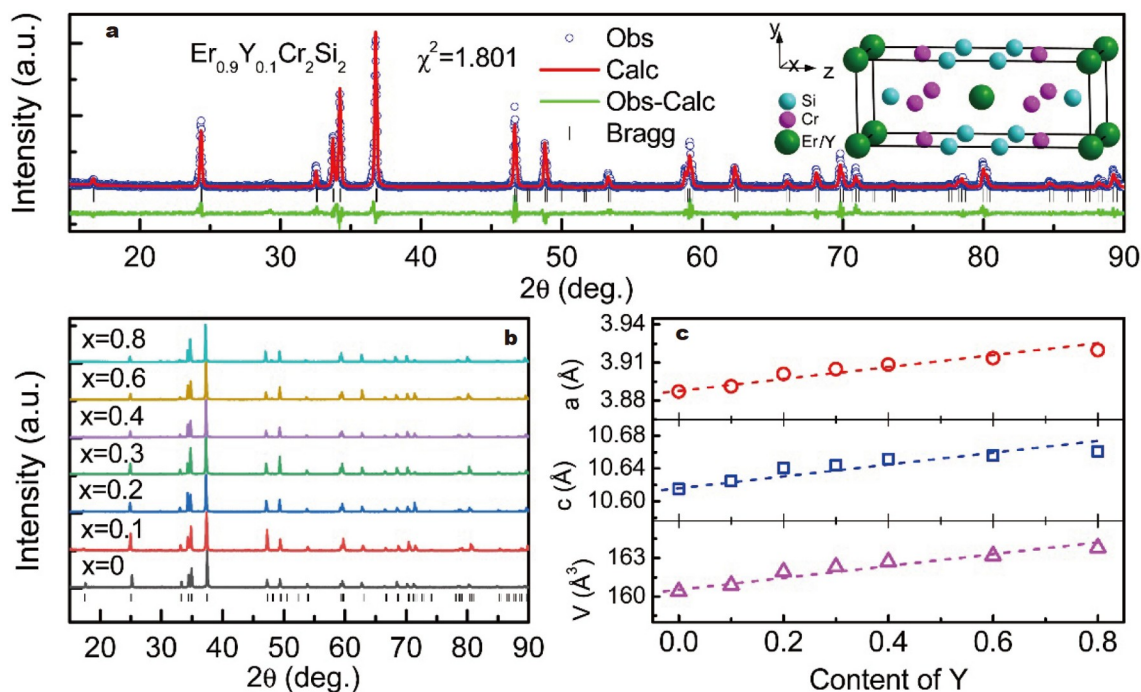
Figure 1 (a) Room-temperature XRD patterns and Rietveld refinement fitting curves of $Er_{0.9}Y_{0.1}Cr_2Si_2$. Inset: the crystal structure of $Er_{0.9}Y_{0.1}Cr_2Si_2$. (b) Powder XRD patterns of $Er_{1-x}Y_xCr_2Si_2$ ($0 \leqslant x \leqslant 0.8$) at room temperature. The vertical bars at the bottom are the referenced Bragg positions of RCr_2Si_2 phase. (c) Y-content dependences of lattice parameters a, c and V for $Er_{1-x}Y_xCr_2Si_2$ ($0 \leqslant x \leqslant 0.8$).

$$2d\sin\theta = n\lambda, \tag{1}$$

where d, θ, λ represent the interplanar spacing, half of diffraction angle and wavelength of X-ray, respectively. Actually, Y-substitution makes the unit cell larger because the radius of Y is larger than that of Er due to the well-known lanthanide contraction.

In order to confirm the homogeneity of the sample, elemental distribution was analyzed for $Er_{0.9}Y_{0.1}Cr_2Si_2$ based on the EDS method. A representative picture of the microstructure for the sample is shown in Fig. 2a and images of the elemental distribution of Er, Y, Cr and Si are presented in Fig. 2b–e, respectively. It can be seen that all the elements are evenly distributed in the field of view, indicating that the selected sample consists of Er, Y, Cr and Si atoms. The EDS spectrum of the sample is shown in Fig. 2f and the atomic ratio of Er, Y, Cr, Si is determined to be 18.31:1.83:40.78:39.07, which is close to the standard atomic ratio of 18:2:40:40 corresponding to the nominal composition. The results of EDS spectrum indicate that the selected piece of sample is the main phase of $Er_{0.9}Y_{0.1}Cr_2Si_2$. To analyze the phase further, HRTEM image was obtained and shown in Fig. 2g. The periodically arranged crystal planes are obviously presented and the interplanar crystal spacing is determined to be 0.192 nm, which can be indexed to the crystal face with the indices of (200). To confirm the congruent relationship between the HR image and the crystal structure, a $5 \times 3 \times 3$ lattice is shown in Fig. 2h along the direction <021>, which is parallel to the crystal plane (200). The d-spacing corresponding to (200) plane is marked in Fig. 2h and the value of d-spacing is calculated to be 0.194 nm, which is in good consistent with the result of Fig. 2g. In addition, a local HR image of $Er_{0.9}Y_{0.1}Cr_2Si_2$ sample is shown in the inset of Fig. 2g. It can be seen that the atomic positions is in good agreement with the crystal structure

of $Er_{0.9}Y_{0.1}Cr_2Si_2$. The above phase analysis of the selected piece of sample indicates that $Er_{0.9}Y_{0.1}Cr_2Si_2$ is of high phase purity.

Magnetic transition, magnetic structure and magnetization behavior

The thermal magnetization curves of $Er_{1-x}Y_xCr_2Si_2$ ($0 \leqslant x \leqslant 0.8$) were measured from 2 to 100 K under the magnetic field of 0.01 T with modes of both zero-field-cooling (ZFC) and FC. As representatives, the ZFC and FC curves are shown in Fig. 3a, b for $Er_{0.9}Y_{0.1}Cr_2Si_2$ and $Er_{0.2}Y_{0.8}Cr_2Si_2$, respectively. It can be seen that the magnetization goes down obviously around 2 K with increasing temperature for $Er_{0.9}Y_{0.1}Cr_2Si_2$ and $Er_{0.2}Y_{0.8}Cr_2Si_2$. However, no drastic point or turning point of magnetization can be observed, indicating of the lower magnetic transition temperature than 2 K. Actually the magnetic transition temperature of $ErCr_2Si_2$ has been reported to be 1.9 K according to HC measurement [35] and the magnetic transition around 2 K is caused by the ferromagnetically coupling Er atoms [34]. It is known that the magnetic exchange interaction between rare earth atoms is positively related to the spin angular momentum quantum number (S) [38]. As the S of Y atom is zero in intermetallic compounds, the magnetic transition temperature of $Er_{1-x}Y_xCr_2Si_2$ ($0 \leqslant x \leqslant 0.8$) is expected to decrease with increasing content of Y. As a result, no transition temperature can be observed for $Er_{1-x}Y_xCr_2Si_2$ ($0 \leqslant x \leqslant 0.8$) in the temperature range between 2 and 100 K. The inset of Fig. 3a shows the enlarged view of ZFC and FC curves of $Er_{0.9}Y_{0.1}Cr_2Si_2$. It is found that the ZFC and FC curves are not overlapped completely around 5 K and similar results are also observed in other $Er_{1-x}Y_xCr_2Si_2$ ($0 \leqslant x \leqslant 0.8$), indicating that $Er_{1-x}Y_xCr_2Si_2$ are not strict paramagnetic (PM) state above 2 K. However, the magnetization behavior at the temperatures above 2 K for
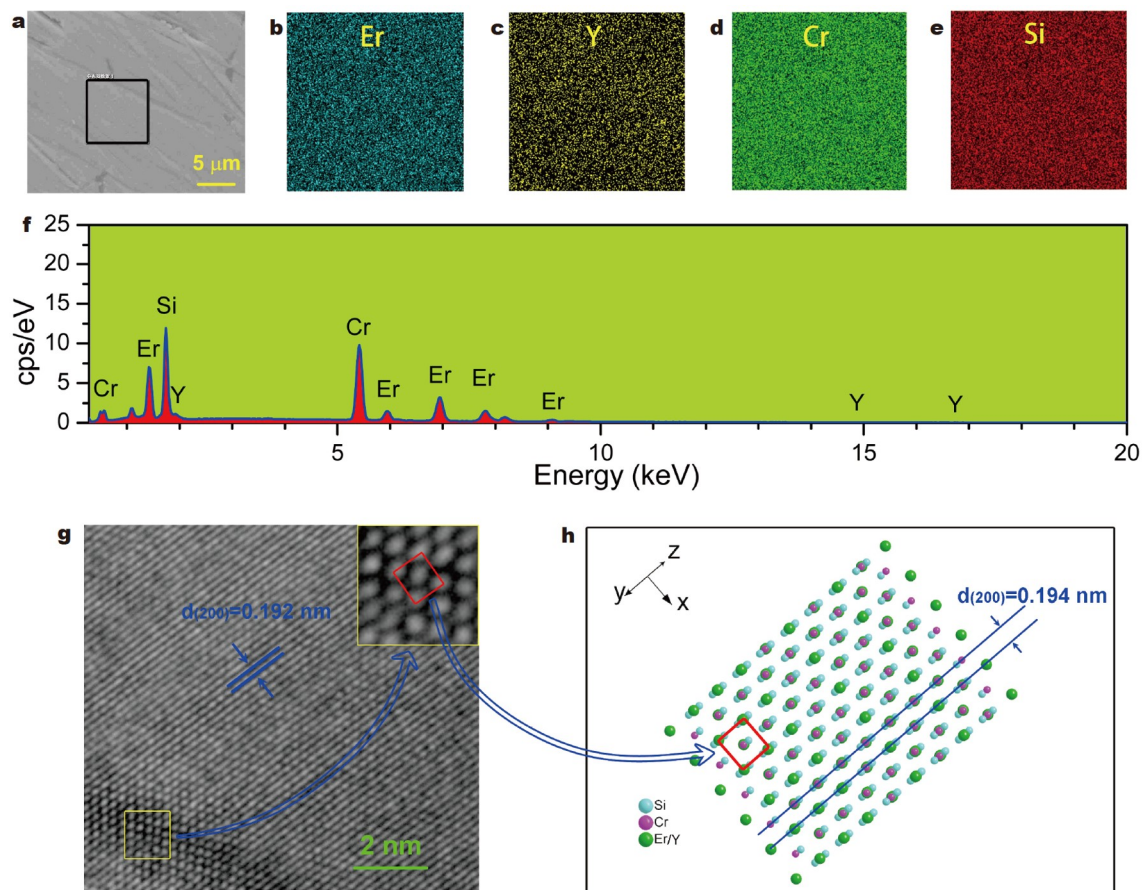
Figure 2 (a) Representative picture of the microstructure for the $Er_{0.9}Y_{0.1}Cr_2Si_2$ sample. Chemical element mappings for (b) Er, (c) Y, (d) Cr and (e) Si in the corresponding area. (f) EDS spectrum of $Er_{0.9}Y_{0.1}Cr_2Si_2$. (g) HR image of the $Er_{0.9}Y_{0.1}Cr_2Si_2$ sample. Inset: enlargement of the selected region of HR image. (h) Sketch map of atom arrangement presented along the direction corresponding to the HR image based on the resolved crystal structure.

$Er_{1-x}Y_xCr_2Si_2$ $(0 \leqslant x \leqslant 0.8)$ is very similar to PM state because the temperature dependence of reciprocal susceptibility can be fitted with a straight line and approximatively obeys Curie-Weiss law as presented in the inset of Fig. 3b. If the Er atom is considered as the only magnetic atom in $Er_{1-x}Y_xCr_2Si_2$ $(0 \leqslant x \leqslant 0.8)$, the atomic magnetic moment of Er can be calculated according to Equation (2).

$$\chi^{-1} = \frac{3k_B(T - \theta_f)}{NM_{eff}^2},\qquad(2)$$

where χ is the magnetic susceptibility, k_B is the Boltzmann constant, θ_f is PM Curie point, N is the number of magnetic atoms and M_{eff} is the effective magnetic moment. It should be pointed that the molecular formula of $Er_{1-x}Y_xCr_2Si_2$ must be normalized to $ErY_{\frac{x}{1-x}}Cr_{\frac{2}{1-x}}Si_{\frac{2}{1-x}}$ before calculation because only the Er atom is assumed to carry magnetic moment. The magnetic moments of Er atoms for $Er_{1-x}Y_xCr_2Si_2$ $(0 \leqslant x \leqslant 0.8)$ are calculated and shown in Fig. 3c and the dotted line indicates the theoretical value of $9.6\mu_B$ for Er atoms [39]. The experimental data are very close to the theoretical value indicating that $Er_{1-x}Y_xCr_2Si_2$ $(0 \leqslant x \leqslant 0.8)$ can be taken as PM state above 2 K approximately. In fact, the experimental phenomenon is in accord with literature [35]. That is to say, even if there is other types of magnetic order above 2 K, it is sure to be very weak. Magnetic transition was also investigated by means of HC measurement from 2 to 100 K at zero field as presented in

Fig. 3d. Though the magnetic transition temperature could not be observed, the upturned curve at low temperatures as shown in the inset of Fig. 3d confirms the magnetic transition is below 2 K, which is in accord with the reported result [35].

In order to confirm if there is other kinds of magnetic order at temperatures above 2 K, the magnetic structure of $Er_{0.9}Y_{0.1}Cr_2Si_2$ was investigated by NPD experiment carried out at 5 K. The diffraction patterns collected by Bank-A, Bank-B and Bank-C and the fitting curves according to Rietveld refinement are shown in Fig. 4a–c, respectively. In the refinement, the sample holder made of vanadium was taken as the secondary phase. All of the fitting curves were calculated by using the phase type of both nuclear and magnetic. Results show that $Er_{0.9}Y_{0.1}Cr_2Si_2$ has the tetragonal crystal structure (space group $I4/mmm$), which is in keeping with the result of XRD experiment. The Rietveld refinement was performed by using program GSAS. The unique symmetry operations and the associated spin colors were set as red, red, black and black for M_z, M_x, $M110$ and $Icen$ respectively. The magnetic moment of Er atoms was set as zero based on the crystal symmetry. Furthermore, according to the requirement of magnetic symmetry, the constraint on the x and y components of magnetic moment for Cr atoms is zero. The z component of M_{Cr} was determined to be $0.9\mu_B$, $0.9\mu_B$ and $0.8\mu_B$ according to the patterns of Bank-A, Bank-B and Bank-C, respectively. To present the contributions of magnetic moments of Cr atoms on the diffraction pattern, enlarged view of the
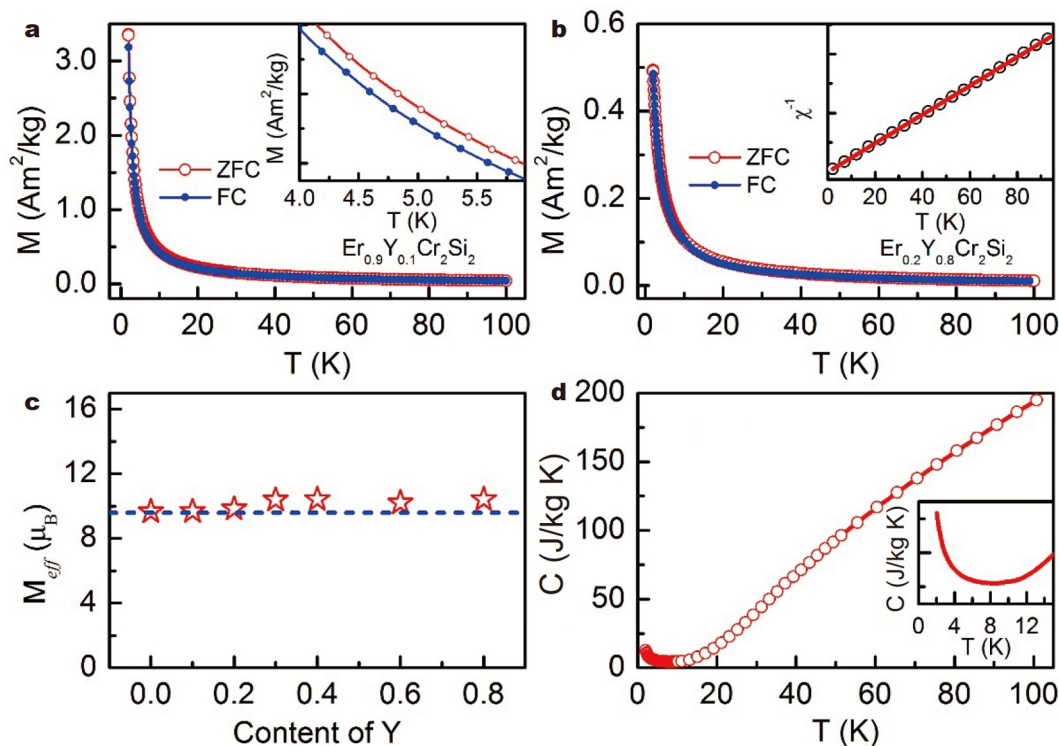
Figure 3 (a) Temperature dependences of the magnetization with the applied field of 0.01 T for $Er_{0.9}Y_{0.1}Cr_2Si_2$. Inset is the enlarged view of ZFC and FC curves. (b) Temperature dependences of the magnetization with the applied field of 0.01 T for $Er_{0.2}Y_{0.8}Cr_2Si_2$. Inset is the linear fitting of the relationship between temperature and reciprocal susceptibility. (c) Y-content dependences of effective magnetic moments for $Er_{1-x}Y_xCr_2Si_2$ ($0 \leqslant x \leqslant 0.8$), where only Er atoms are considered as magnetic atoms. (d) Temperature dependences of specific heat for $Er_{0.9}Y_{0.1}Cr_2Si_2$ at 0 T. Inset: the specific heat curve at low temperatures.

fitting curves around peak (211) based on the nuclear only model and nuclear & magnetic model are shown in Fig. 4d, e, respectively. For the nuclear only model, the weak diffraction pattern of (211) as shown in Fig. 4d completely originates from rare earth atoms and Si atoms, because the contribution of 4d sites occupied by Cr atoms is zero with the reflection condition of $l = 2n$, where l is the third crystal index and n is integer. However, when the magnetic contribution of Cr atoms is considered, which will be confirmed as antiferromagnetic (AFM) order, the calculated diffraction signals are enhanced as presented in Fig. 4e. Obviously, the model of nuclear & magnetic is more reasonable to describe the structure of $Er_{0.9}Y_{0.1}Cr_2Si_2$. In fact, the magnetic structure of $ErCr_2Si_2$ has been investigated based on neutron diffraction experiment at 2 K [34]. The magnetic structure is redrawn in Fig. 4f with Er atoms FM ordering along the y axis and Cr atoms AFM ordering along the direction of z axis. For $Er_{0.9}Y_{0.1}Cr_2Si_2$ at 5 K, the detailed magnetic moments are also derived from the results of fitting and the magnetic structure is shown in Fig. 4g. It can be seen that $Er_{0.9}Y_{0.1}Cr_2Si_2$ is not PM state but AFM ordered at 5 K and the alignment of M_{Cr} in $Er_{0.9}Y_{0.1}Cr_2Si_2$ has the same form as that in $ErCr_2Si_2$. Since the constructing of magnetic ordering as cooling and the deconstructing of magnetic ordering as warming experience different levels of obstruction due to kinds of factors such as crystal defect, crystal boundary and magnetic anisotropy, the ZFC and FC curves are not overlapped completely as presented in the inset of Fig. 3a. It can also be understood that $Er_{0.9}Y_{0.1}Cr_2Si_2$ can be approximately taken as PM state to calculate effective magnetic moment and obtain reasonable values.

Because the magnetic moment of Cr atoms above 2 K is determined to be only about $0.9\mu_B$, which is much smaller compared with the effective magnetic moment of Er atoms.

To further investigate the magnetic properties of $Er_{1-x}Y_xCr_2Si_2$ ($0 \leqslant x \leqslant 0.8$), isothermal magnetization curves were measured with the applied magnetic field up to 7 T at temperatures from 2 to 36/40 K (Figs S1–S7). The isothermal magnetization curve at 2 K for $Er_{0.9}Y_{0.1}Cr_2Si_2$ is shown in Fig. 5a. Magnetization goes up quickly with increasing magnetic field and reaches its saturation value approximately with magnetic field increasing further, which is similar to the characteristic of FM ground state. However, the first differential of magnetization as presented in Fig. 5a indicates that there is a maximum value around 0.1 T, which is the typical feature of AFM ground state. It is in good accordance with the result of NPD experiment and the AFM ordering originates from the antiparallel magnetic moments of Cr atoms. Even if the ground state is AFM, it still saturates quickly with increasing magnetic field, because the AFM ordering is very weak. The saturated magnetic field is estimated as 0.42 T as shown in Fig. 5a. Furthermore, the saturated magnetic fields for all of the $Er_{1-x}Y_xCr_2Si_2$ ($0 \leqslant x \leqslant 0.8$) compounds are obtained and the Y-content dependence of saturated magnetic field is presented in Fig. 5b. It is found that saturated filed changes without monotonous trend with increasing content of Y and it shows the minimal value corresponding to the $Er_{0.9}Y_{0.1}Cr_2Si_2$ sample. That is to say, $Er_{0.9}Y_{0.1}Cr_2Si_2$ can be magnetized to saturated value more easily compared with other $Er_{1-x}Y_xCr_2Si_2$ compounds.

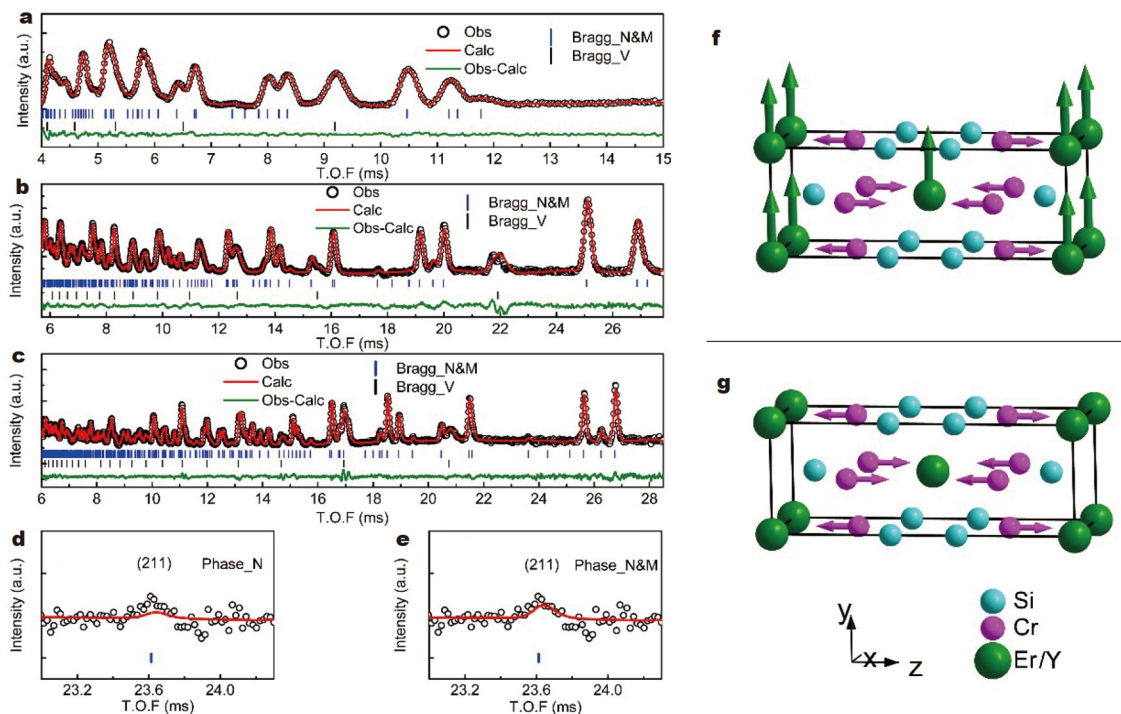Experimental saturation magnetic moment (M_S^{Exp}) at 2 K is

Figure 4 NPD patterns of $Er_{0.9}Y_{0.1}Cr_2Si_2$ measured at 5 K along with Rietveld refinement fitting curves, Bragg positions of different phases and the differences between observed data and calculated values carried out on (a) Bank-A, (b) Bank-B, and (c) Bank-C, respectively. Enlarged view of fitting curves based on the data collected by Bank-C with only nuclear model (d) and nuclear & magnetic model (e), respectively. (f) Reported magnetic structure of $ErCr_2Si_2$ at 2 K. (g) Resolved magnetic structure of $Er_{0.9}Y_{0.1}Cr_2Si_2$ at 5 K.

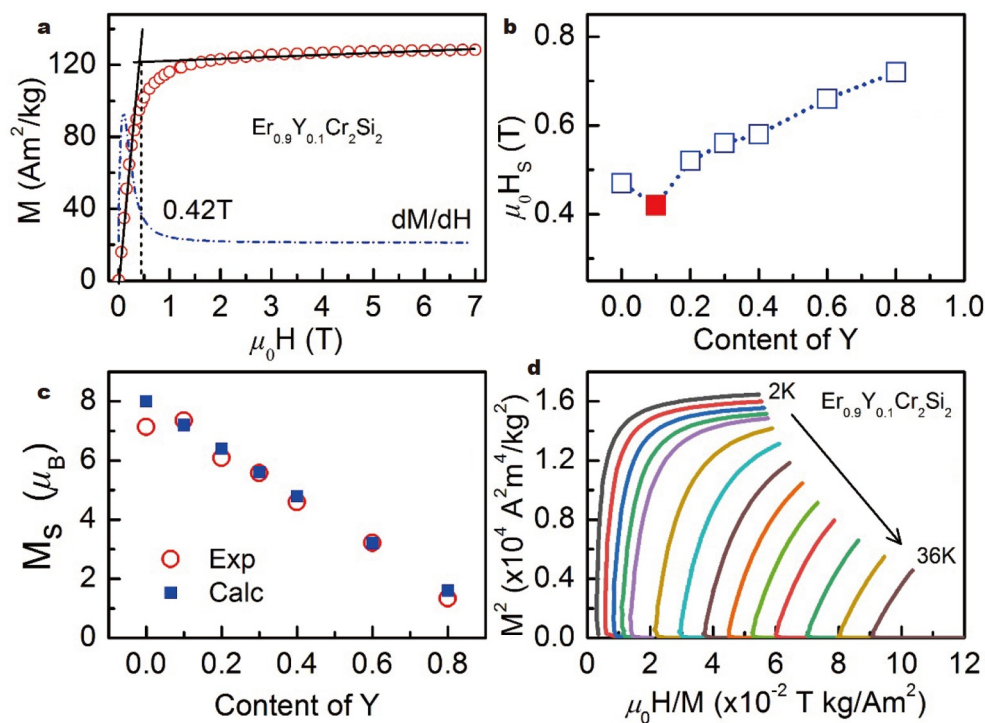**Figure 5** (a) The hollow circle represents the isothermal magnetization measured at 2 K with applied fields up to 7 T for $Er_{0.9}Y_{0.1}Cr_2Si_2$. The dotted line represents the first-order derivative of MH curve. The cross point between the two solid lines represents the saturation field. (b) Y-content dependence of the saturation field. (c) Y-content dependences of the saturation magnetic moments and theoretical values for $Er_{1-x}Y_xCr_2Si_2$ $(0 \leqslant x \leqslant 0.8)$. (d) Arrott plots of $Er_{0.9}Y_{0.1}Cr_2Si_2$.

also obtained based on the isothermal magnetization curve for $Er_{1-x}Y_xCr_2Si_2$ ($0 \leqslant x \leqslant 0.8$). Since the saturated magnetic fields are all lower than 0.8 T according to Fig. 5b and the samples have already been saturated when the magnetic field adds up to 7 T, the M_S^{Exp} is estimated by M_{7T} approximately, where M_{7T} is the value of magnetization measured at the field of 7 T. The specific value of M_S^{Exp} corresponding to each $Er_{1-x}Y_xCr_2Si_2$ sample is shown in Fig. 5c. In addition, saturation magnetic moment can also be calculated based on the experimental value of the Er atom ($M_S^{Er} = 8\mu_B$) following Equation (3) assuming that the contribution of Cr on M_S^{Exp} is negligible and it is marked as M_S^{Calc}.

$$M_S^{Calc} = 8(1-x)\mu_B, \tag{3}$$

where x is the content of Y in $Er_{1-x}Y_xCr_2Si_2$. The experimental value is in good accordance with the calculated value for most of $Er_{1-x}Y_xCr_2Si_2$ compounds except $ErCr_2Si_2$, which further confirms that the contribution on saturated magnetic moment mainly originates from Er atoms. It should be noted that $Er_{0.9}Y_{0.1}Cr_2Si_2$ shows the largest M_S^{Exp} among the $Er_{1-x}Y_xCr_2Si_2$ ($0 \leqslant x \leqslant 0.8$) compounds. The result indicates that $Er_{0.9}Y_{0.1}Cr_2Si_2$ can be magnetized to a higher ordered magnetic state because saturation magnetization is a good evaluation for the degree of magnetic order.

Arrott plots are usually used to determine the order of magnetic transitions according to the Inoue-Shimizu model [40]. It is known that a magnetic system with an applied magnetic field (H) can be described by Landau expansion of the free energy (F) in powers of magnetization (M) as described in Equation (4) [41].

$$F(M,T) = \frac{C_1(T)}{2}M^2 + \frac{C_3(T)}{4}M^4 + \frac{C_5(T)}{6}M^6 + \cdots \tag{4}$$
$$+ \mu_0 HM,$$

where C_1, C_3, C_5 are Landau coefficients. Then the Landau coefficients are accessible through the equation of state linking M and $\mu_0 H$ as Equation (5).

$$\mu_0 H = C_1(T)M + C_3(T)M^3 + C_5(T)M^5. \tag{5}$$

Furthermore, Landau coefficient C_3 can be obtained by examining the dependency relationship between $\mu_0 H/M$ and M^2 on basis of Equation (6).

$$M^2 = \frac{1}{C_3(T)}\frac{\mu_0 H}{M} - \frac{C_1(T)}{C_3(T)} - \frac{C_5(T)}{C_3(T)}M^4. \tag{6}$$

Especially, the sign of C_3 can be determined easily by investigating the slope of Arrott plots. It was known that if Landau coefficient C_3 is negative near the transition temperature, the magnetic transition is considered to be of first order and if else, it is of second order. The orders of magnetic transition for $Er_{1-x}Y_xCr_2Si_2$ ($0 \leqslant x \leqslant 0.8$) are all investigated based on Arrott plots. Taking $Er_{0.9}Y_{0.1}Cr_2Si_2$ as an example as presented in Fig. 5d, it can be seen that the slopes are all positive, indicating of the second-order magnetic transition. It should be noticed that MCE materials of second order is expected to have good thermal and magnetic reversibility, which is of great importance to the practical applications. It should also be pointed out that Arrott plot is the most commonly used method to determine the type of magnetic transitions. However, it is found that some

magnetic system is so complicated that Arrott plot is not accurate enough to deduce the order of magnetic transition [27]. Therefore, as for this series, the type of magnetic transitions is also studied by other methods, which will be discussed later.

Giant low-field MCE

The isothermal entropy change (ΔS_M) is the most frequently used parameter to evaluate the performance of MCE materials. ΔS_M of $Er_{1-x}Y_xCr_2Si_2$ ($0 \leqslant x \leqslant 0.8$) was calculated based on the isothermal magnetization data and Maxwell relationship as described by Equation (7).

$$\Delta S_M(T,B) = \int_0^{B_f} \left(\frac{\partial M}{\partial T}\right)_H dB, \tag{7}$$

where B_f is the final magnetic field corresponding to ΔS_M. In consideration that the magnetization data are collected with separated temperatures and magnetic fields, the above integral formula can be transformed as Equation (8) approximately.

$$\Delta S_M(T,B) = \sum_i \frac{1}{2\Delta T}(M_i^{T-\Delta T} - M_i^{T+\Delta T})\Delta B, \tag{8}$$

where ΔT is the interval of temperature at which isothermal magnetization data are collected. $M_i^{T-\Delta T}$ and $M_i^{T+\Delta T}$ are the magnetizations measured at each magnetic field with appropriate steps corresponding to $T - \Delta T$ and $T + \Delta T$, respectively. The Y-content dependences of maximum value of $-\Delta S_M$ (($-\Delta S_M)_{max}$) under the field changes of 0–1, 0–2, 0–5 and 0–7 T are presented in Fig. 6a. Taking the curve under the field change of 0–1 T as an example, the value of ($-\Delta S_M)_{max}$ goes up with increasing Y-content and it then goes down with further increasing Y-content when x exceeds 0.1. That is to say, $Er_{0.9}Y_{0.1}Cr_2Si_2$ shows the maximum value of ($-\Delta S_M)_{max}$ among $Er_{1-x}Y_xCr_2Si_2$ ($0 \leqslant x \leqslant 0.8$). It is further found that the variation trend of ($-\Delta S_M)_{max}$ with increasing Y-content is consistent for different field changes. The detailed ($-\Delta S_M)_{max}$ parameters of $Er_{1-x}Y_xCr_2Si_2$ ($0 \leqslant x \leqslant 0.8$) as well as some low-temperature magnetocaloric materials (including HoB_2 [12], $ErMn_2Si_2$ [17], EuS [13], TmGa [42], TmCuAl [43], TmCoSi [15], TmZn [44], ErNiBC [45], $TmMn_2Si_2$ [46], and HoNiSi [47]) for field changes of 0–1 and 0–5 T have been listed in Table 1. It is found that $Er_{1-x}Y_xCr_2Si_2$ ($0 \leqslant x \leqslant 0.8$) shows large/giant magnetic entropy changes and the value of ($-\Delta S_M)_{max}$ is comparable to or even larger than that of other series. It should be pointed out that the ($-\Delta S_M)_{max}$ of $Er_{0.9}Y_{0.1}Cr_2Si_2$ under 0–1 T is much larger than those of other low-temperature magnetic refrigerant materials. Compared with $ErCr_2Si_2$, the value of ($-\Delta S_M)_{max}$ for $Er_{0.9}Y_{0.1}$-Cr_2Si_2 shows an enhancement of 15.7% and 19.0% under the field changes of 0–1 and 0–5 T, respectively. The physical mechanism about the great enhancement due to Y substitution originates from the larger saturation magnetic moments and the smaller saturated magnetic fields. The temperature dependences of ($-\Delta S_M$) for $Er_{0.9}Y_{0.1}Cr_2Si_2$ are presented in Fig. 6b for field changes of 0–1, 0–2, 0–3, 0–4, 0–5, 0–6 and 0–7 T, respectively. Since the ordering temperature of Er atoms is below 2 K, the main peak of ($-\Delta S_M$) curve could not be observed for 0–1 and 0–2 T. As a matter of fact, the corresponding value of ($-\Delta S_M)_{max}$ shown in Table 1 and Fig. 6a is approximately described by the value of ($-\Delta S_M$) at the lowest calculated temperature of 2.5 K. It can also be seen that there is a bulge on the ($-\Delta S_M$) curve under high field changes such as 0–5, 0–6 and 0–7 T around 12 K.
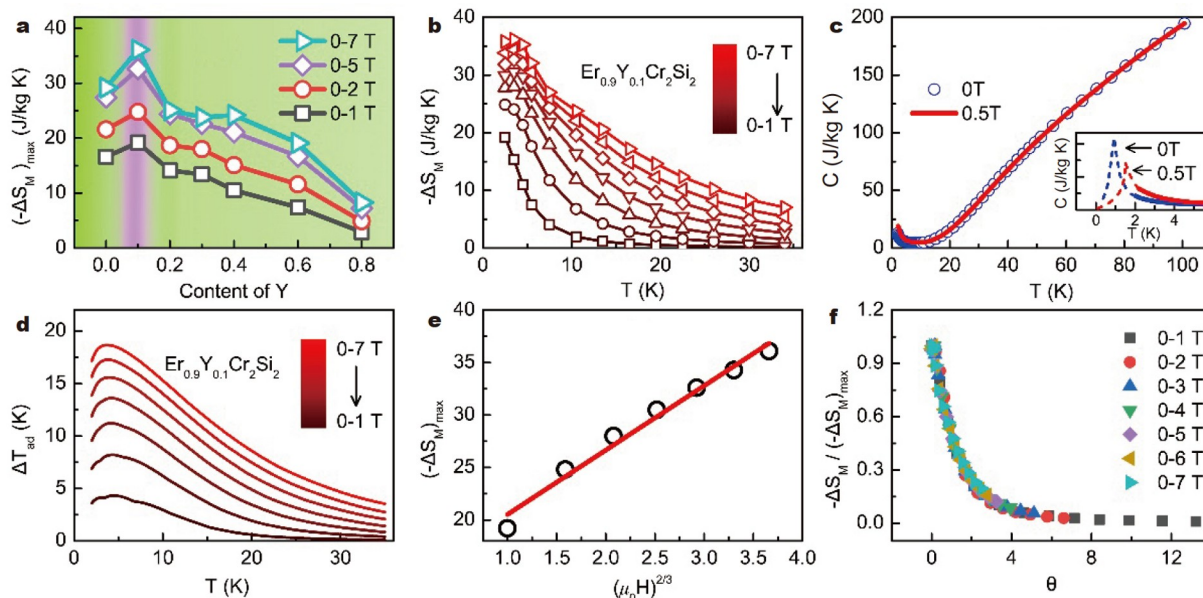
Figure 6 (a) Y-content dependences of $(-\Delta S_M)_{max}$ for field changes of 0–1, 0–2, 0–5 and 0–7 T, respectively. (b) Temperature dependences of magnetic entropy change $(-\Delta S_M)$ for $Er_{0.9}Y_{0.1}Cr_2Si_2$ under field changes of 0–1, 0–2, 0–3, 0–4, 0–5, 0–6 and 0–7 T, respectively. (c) Temperature dependences of HC under the fields of 0 and 0.5 T for $Er_{0.9}Y_{0.1}Cr_2Si_2$. (d) Temperature dependences of adiabatic temperature change ΔT_{ad} for $Er_{0.9}Y_{0.1}Cr_2Si_2$ under field changes of 0–1, 0–2, 0–3, 0–4, 0–5, 0–6 and 0–7 T, respectively. (e) Linear fitting of the relationship between $(-\Delta S_M)_{max}$ and $(\mu_0 H)^{2/3}$. (f) Rescaled $(-\Delta S_M)$ curves for $Er_{0.9}Y_{0.1}Cr_2Si_2$.

Table 1 Magnetic ordering temperatures, $(-\Delta S_M)_{max}$ and $(\Delta T_{ab})_{max}$ of $Er_{1-x}Y_xCr_2Si_2$ compounds and typical low-temperature MCE materials

Samples	T_C/T_N	$-\Delta S_M^{max}$ (J kg^{-1} K^{-1})		ΔT_{ad}^{max}		Ref.
		0–1 T	0–5 T	0–1 T	0–5 T	
$ErCr_2Si_2$	[a]	16.6	27.4	–	–	This work
$Er_{0.9}Y_{0.1}Cr_2Si_2$	[a]	19.2	32.6	4.3	15.6	This work
$Er_{0.8}Y_{0.2}Cr_2Si_2$	[a]	14.1	24.4	–	–	This work
$Er_{0.7}Y_{0.3}Cr_2Si_2$	[a]	13.4	22.6	–	–	This work
$Er_{0.6}Y_{0.4}Cr_2Si_2$	[a]	10.5	21.1	–	–	This work
$Er_{0.4}Y_{0.6}Cr_2Si_2$	[a]	7.4	16.7	–	–	This work
$Er_{0.2}Y_{0.8}Cr_2Si_2$	[a]	2.9	7.2	–	–	This work
HoB_2	15	14.9[b]	40.1	3.4[b]	12.0	[12]
$ErMn_2Si_2$	6.6	14.7	25.2	2.5	12.9	[17]
EuS	18.2	13.5[a]	37	–	10.4	[13]
TmGa	15.0	12.9	34.2	3.2	9.1	[42]
TmCuAl	2.8	12.2	24.3	–	9.4	[43]
TmCoSi	4.4	12.0	22.1	6.2	17.3	[15]
TmZn	8	11.8	26.9	–	8.6	[44]
ErNiBC	5.0	9.8	24.8	2.7	8.6	[45]
$TmMn_2Si_2$	5.5	9.5	22.7	2.7	10.1	[46]
HoNiSi	3.8	9.3	26	–	8.5	[47]

a) The magnetic ordering temperatures were not available according to magnetic measurements from 2 K. b) These results are estimated from the relevant references.

However, no obvious bulge can be observed under field changes of 0–1, 0–2 and 0–3 T. It has been demonstrated that AFM Cr ordering exists at temperatures above 2 K according to NPD experiments and magnetic measurements. Since the AFM ordering is very weak, the change of magnetic ordering under low field change is not as obvious as that under high field change.

To investigate the magnetic transitions further for $Er_{0.9}Y_{0.1}$-Cr_2Si_2, temperature dependences of HC at 0 and 0.5 T from 2 to 100 K were measured and shown in Fig. 6c. Since the magnetic ordering temperature of Er atoms is lower than 2 K, no peaks is observed on the curves at 0 and 0.5 T. The specific heat curves almost overlap completely at high temperatures, indicating that the magnetic field has an negligible influence on the HC as well

as magnetic ordering in the corresponding temperature range. It is noticed that the value of specific heat goes up with decreasing temperature around 2 K at the magnetic field of 0 T, which is not in accord with the classical description of specific heat as $\gamma T + bT^3$ for solid state systems. That is because the contribution of magnetic ordering on specific heat becomes obvious around 2 K while the contribution of electron and lattice vibration gets insignificant. And a peak on the specific heat curve is expected at the temperatures below 2 K. It can also be seen that the specific heat under 0.5 T is higher than that under 0 T at low temperatures such as 2 K as presented in the inset of Fig. 6c. In order to interpret the above result, the estimated specific heat curves below 2 K at 0 and 0.5 T are also plotted roughly and qualitatively in the inset of Fig. 6c. It is known that the peak on the specific heat curve around the magnetic transition temperature will move toward higher temperatures for magnetic materials because the magnetic field can break the balance between magnetic coupling and thermal vibration and push the critical temperature to a higher temperature region. Considering that the peaks for 0 and 0.5 T are both below 2 K as shown in the inset of Fig. 6c, it is not difficult to understand that the specific heat at 2 K for 0.5 T is higher than that for 0 T.

Adiabatic temperature change (ΔT_{ad}) is another important parameter to evaluate the MCE of magnetic materials. The ΔT_{ad} is calculated by the methods as follows: first, temperature dependence of zero-field entropy ($S(T,\mu_0 H = 0T)$) is calculated based on the specific heat data at 0 T according to Equation (9). Second, temperature dependence of none-zero-field entropy ($S(T,\mu_0 H)$) is calculated based on zero-field entropy and ΔS_M according to Equation (10). Third, temperature dependences of entropy ($S(T,\mu_0 H)$) are transferred to entropy dependence of temperature ($T(S,\mu_0 H)$) according to the transformation of inverse function. Finally, temperature dependences of ΔT_{ad} are obtained by subtracting the zero-field entropy dependence of temperature from the none-zero-field entropy dependence of temperature according to Equation (11).

$$S(T, 0T) = \int_{2K}^{T} \frac{C(T', 0T)}{T'} dT',\qquad(9)$$

$$S\left(T, \mu_0 H\right) = S(T, 0T) + \Delta S_M(T, 0T \rightarrow \mu_0 H),\qquad(10)$$

$$\Delta T\left(T, 0T \rightarrow \mu_0 H\right) = T\left(S, \mu_0 H\right) - T(S, 0T).\qquad(11)$$

The temperature dependences of ΔT_{ad} for $Er_{0.9}Y_{0.1}Cr_2Si_2$ under field changes of 0–1, 0–2, 0–3, 0–4, 0–5, 0–6 and 0–7 T were calculated and presented in Fig. 6d, respectively. The patterns of ΔT_{ad} curves are similar to those of $-\Delta S_M$ curves and peaks are not obvious for low field changes. The maximum of adiabatic temperature change (($\Delta T_{ad})_{max}$) is observed around 2 K and specific values are determined to be 4.3, 8.2, 11.2, 13.6, 15.6, 17.3 and 18.7 K correspondingly. To compare the ΔT_{ad} of $Er_{0.9}Y_{0.1}Cr_2Si_2$ with other representative low-temperature magnetocaloric materials, the ($\Delta T_{ad})_{max}$ under 0–1 and 0–5 T is also listed in Table 1. It can be seen that $Er_{0.9}Y_{0.1}Cr_2Si_2$ shows obvious advantages on ($\Delta T_{ad})_{max}$ in comparison with most low-temperature magnetocaloric materials except for TmCoSi whether the field change is 0–1 or 0–5 T. The excellent performance of adiabatic temperature change of $Er_{0.9}Y_{0.1}Cr_2Si_2$ indicates the vast potential for future applications in low-temperature magnetic refrigeration.

As magnetic refrigerant materials, the characteristic of magnetic transition is of vital importance for the applications and the feature of second order has been demonstrated according to Arrott plots for $Er_{0.9}Y_{0.1}Cr_2Si_2$. However, for some cases, it is not accurate to confirm the second-order magnetic phase transition according to Arrott plots [48]. To further analyze the characteristic of magnetic transition of $Er_{0.9}Y_{0.1}Cr_2Si_2$, the power law method and rescaled universal $-\Delta S_M$ curve method are used. According to the mean field theory, the value of ($-\Delta S_M)_{max}$ is proportionate to the 2/3 power of the change of magnetic field if the magnetic transition is of second order. The ($\mu_0 H)^{2/3}$ dependence of ($-\Delta S_M)_{max}$ is plotted in Fig. 6e for $Er_{0.9}Y_{0.1}Cr_2Si_2$ and the scattering points can be fitted by a straight line, indicating that the power law is appropriate in the system. According to the rescaled universal $-\Delta S_M$ curve method [49], the $-\Delta S_M$ curves for different field changes are normalized as $-\Delta S_M/(-\Delta S_M)_{max}$ and the temperatures were normalized as Equation (12):

$$\theta = \begin{cases} -\dfrac{T - T_C}{T_{r1} - T_C}, (T \leqslant T_C), \\[2mm] \dfrac{T - T_C}{T_{r2} - T_C}, (T > T_C), \end{cases}\qquad(12)$$

where T_{r1} and T_{r2} are reference temperatures and they are usually selected as the ones corresponding to the half of $|(\Delta S_M)_{max}|$. If the magnetic system is of second order, the rescaled $-\Delta S_M$ curves will overlap with each other. The detailed normalized $-\Delta S_M$ curves of $Er_{0.9}Y_{0.1}Cr_2Si_2$ for different field changes are presented in Fig. 6f and it can be obviously seen that all the curves coincide into one universal curve, which is in accord with the description of second-order magnetic transition. That is to say, the above two methods further confirm the characteristic of second-order magnetic transition for $Er_{0.9}Y_{0.1}Cr_2Si_2$. As a result, good thermal and magnetic reversibility is expected as a refrigerant material.

To evaluate the MCE performance further, the ($-\Delta S_M)_{max}$ of Er-Y-Cr-Si series and the representative low-temperature magnetic refrigerant materials under the field changes of 0–1 and 0–5 T are shown in Fig. 7a, b, respectively. It is clear that though the ($-\Delta S_M)_{max}$ of Er-Y-Cr-Si series under field change of 0–5 T is moderate among low-temperature magnetic refrigerant materials, the ($-\Delta S_M)_{max}$ under field change of 0–1 T has advanced competitiveness. That is because Er-Y-Cr-Si series have the saturated magnetic field lower than 1 T in general according to magnetic measurements. More importantly, the value of ($-\Delta S_M)_{max}$ under field change of 0–1 T for $Er_{0.9}Y_{0.1}Cr_2Si_2$ is as high as 19.2 J kg^{-1} K^{-1}, which is the largest value among the ever reported intermetallic magnetocaloric materials with working temperatures below 20 K. It is known that low-field MCE is of great importance to practical applications of magnetic refrigerant materials. That is to say, $Er_{0.9}Y_{0.1}Cr_2Si_2$ shows giant low-field magnetic entropy change and is of huge value for applications at low temperatures.

It has been mentioned that $Er_{1-x}Y_xCr_2Si_2$ ($0 \leqslant x \leqslant 0.8$) show large/giant MCE and $Er_{0.9}Y_{0.1}Cr_2Si_2$ has the most excellent performance among $Er_{1-x}Y_xCr_2Si_2$ ($0 \leqslant x \leqslant 0.8$). Therefore, it is necessary to further analyze the reason why $Er_{0.9}Y_{0.1}Cr_2Si_2$ shows the largest ($-\Delta S_M)_{max}$ among the Er-Y-Cr-Si series and discuss the giant low-field $-\Delta S_M$ of $Er_{0.9}Y_{0.1}Cr_2Si_2$. Generally to say, the value of ($-\Delta S_M)_{max}$ around the transition temperature can be expressed as Equation (13) according to Oesterreicher et al. [50].
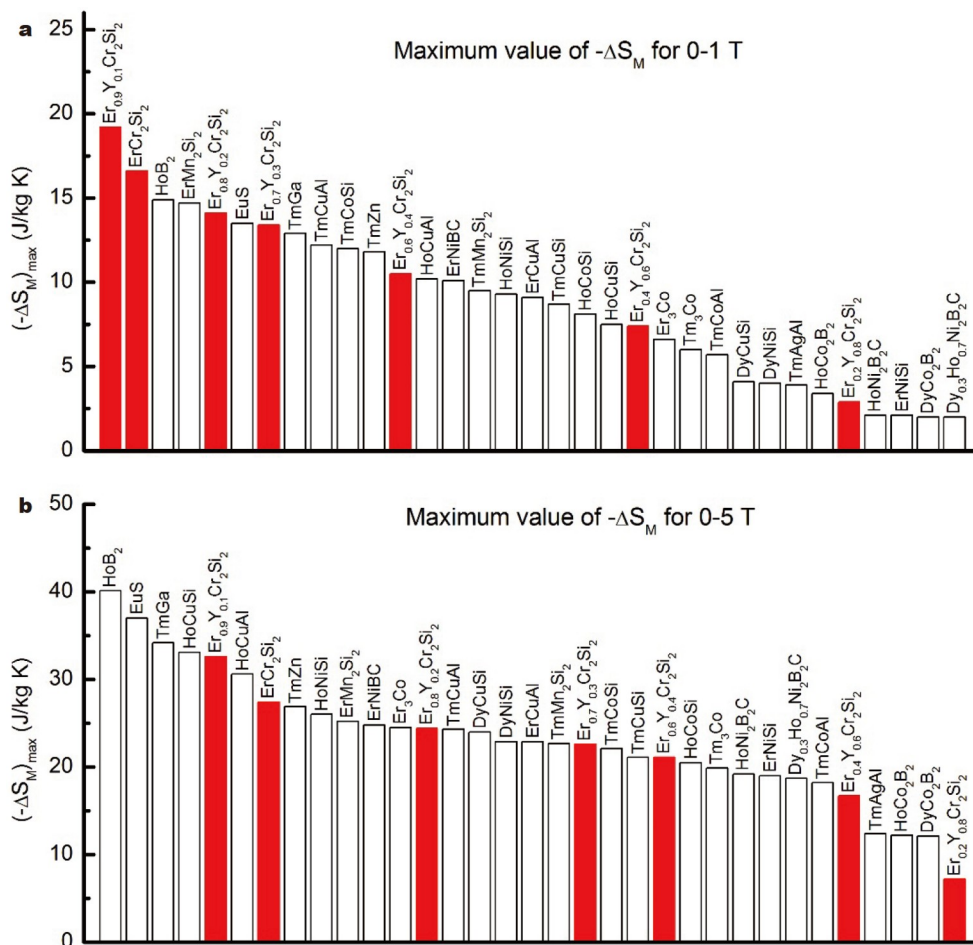
Figure 7 Comparison of $(-\Delta S_M)_{max}$ for field changes of (a) 0–1 and (b) 0–5 T between $Er_{1-x}Y_xCr_2Si_2$ compounds and typical intermetallic low-temperature MCE materials with working temperatures below 20 K.

$$(-\Delta S_M)_{max} \approx 1.07nR\left(\frac{g\mu_B JH}{kT_0}\right)^{2/3}, \tag{13}$$

where n, R, g, J, k, and T_0 are the mole number, universal gas constant, Lande factor, total angular momentum quantum number, Boltzmann constant, and ordering temperature, respectively. It is known that $gJ\mu_B$ is the theoretical saturation magnetization (M_S) of a magnetic system and the magnetic ordering temperatures of Er-Y-Cr-Si series are close to each other. As a result, the value of $(-\Delta S_M)_{max}$ is positively related to the M_S of $Er_{1-x}Y_xCr_2Si_2$ ($0 \leqslant x \leqslant 0.8$). Since the experimental M_S of $Er_{0.9}Y_{0.1}Cr_2Si_2$ is larger than that of other $Er_{1-x}Y_xCr_2Si_2$ compounds according to MH data, $Er_{0.9}Y_{0.1}Cr_2Si_2$ shows the largest $(-\Delta S_M)_{max}$ among Er-Y-Cr-Si series. MCE under low field changes is closely associated with the magnetizing process, which can be well evaluated by the saturated field. It has been analyzed that $Er_{0.9}Y_{0.1}Cr_2Si_2$ shows the lowest saturated field, which further leads to the largest magnetic entropy change for low field changes such as 0–1 T.

CONCLUSIONS

In summary, $Er_{1-x}Y_xCr_2Si_2$ ($0 \leqslant x \leqslant 0.8$) are synthesized and the influence of Y-substitution on the crystal structure, magnetic structure, magnetic transition and MCE is investigated in detail. It is found that Y-substitution does not change the type of crystal structure and magnetic structure. $Er_{0.9}Y_{0.1}Cr_2Si_2$ shows the lar-

gest saturation magnetization and lowest saturated magnetic field among the $Er_{1-x}Y_xCr_2Si_2$ compounds. Large MCEs are obtained in $Er_{1-x}Y_xCr_2Si_2$ series, among which $Er_{0.9}Y_{0.1}Cr_2Si_2$ shows the best low-field MCE performance. Under the filed change of 0–1 T, the value of $(-\Delta S_M)_{max}$ is calculated to be 19.2 J kg^{-1} K^{-1}, which is the largest value ever reported for intermetallic MCE materials below 20 K. The physical mechanism about the great enhancement due to Y substitution originates from the larger saturation magnetic moments and the smaller saturated magnetic fields.

1   Moya X, Mathur ND. Caloric materials for cooling and heating. Science, 2020, 370: 797–803
2   Hou H, Qian S, Takeuchi I. Materials, physics and systems for multicaloric cooling. Nat Rev Mater, 2022, 7: 633–652
3   Gottschall T, Gràcia-Condal A, Fries M, et al. A multicaloric cooling cycle that exploits thermal hysteresis. Nat Mater, 2018, 17: 929–934
4   Pecharsky VK, Gschneidner K.~A. J, Pecharsky AO, et al. Thermodynamics of the magnetocaloric effect. Phys Rev B, 2001, 64: 144406
5   Pecharsky VK, Gschneidner Jr KA. Giant magnetocaloric effect in Gd$_5$(Si$_2$Ge$_2$). Phys Rev Lett, 1997, 78: 4494–4497
6   Hu F, Shen B, Sun J, et al. Influence of negative lattice expansion and metamagnetic transition on magnetic entropy change in the compound LaFe$_{11.4}$Si$_{1.6}$. Appl Phys Lett, 2001, 78: 3675–3677
7   Cong D, Xiong W, Planes A, et al. Colossal elastocaloric effect in fer-

roelastic Ni–Mn–Ti alloys. Phys Rev Lett, 2019, 122: 255703

8   Krenke T, Duman E, Acet M, *et al.* Inverse magnetocaloric effect in ferromagnetic Ni–Mn–Sn alloys. Nat Mater, 2005, 4: 450–454

9   Wada H, Tanabe Y. Giant magnetocaloric effect of $MnAs_{1-x}Sb_x$. Appl Phys Lett, 2001, 79: 3302–3304

10 Tegus O, Brück E, Buschow KHJ, *et al.* Transition-metal-based magnetic refrigerants for room-temperature applications. Nature, 2002, 415: 150–152

11 Giguere A, Foldeaki M, Schnelle W, *et al.* Metamagnetic transition and magnetocaloric effect in $ErCo_2$. J Phys-Condens Matter, 1999, 11: 6969–6981

12 Castro PB, Terashima K, Yamamoto TD, *et al.* Machine-learning-guided discovery of the gigantic magnetocaloric effect in HoB_2 near the hydrogen liquefaction temperature. NPG Asia Mater, 2020, 12: 35

13 Li DX, Yamamura T, Nimori S, *et al.* Large reversible magnetocaloric effect in ferromagnetic semiconductor EuS. Solid State Commun, 2014, 193: 6–10

14 Guillou F, Pathak AK, Paudyal D, *et al.* Non-hysteretic first-order phase transition with large latent heat and giant low-field magnetocaloric effect. Nat Commun, 2018, 9: 2925

15 Xu JW, Zheng XQ, Yang SX, *et al.* Giant low field magnetocaloric effect in TmCoSi and TmCuSi compounds. J Alloys Compd, 2020, 843: 155930

16 Zheng XQ, Zhang B, Wu H, *et al.* Large magnetocaloric effect of $Ho_xEr_{1-x}Ni$ ($0 \leqslant x \leqslant 1$) compounds. J Appl Phys, 2016, 120: 163907

17 Li L, Nishimura K, Hutchison WD, *et al.* Giant reversible magnetocaloric effect in $ErMn_2Si_2$ compound with a second order magnetic phase transition. Appl Phys Lett, 2012, 100: 152403

18 Zhang Y, Zhu J, Li S, *et al.* Magnetic properties and promising magnetocaloric performances in the antiferromagnetic $GdFe_2Si_2$ compound. Sci China Mater, 2022, 65: 1345–1352

19 Guo D, Moreno-Ramírez LM, Law JY, *et al.* Excellent cryogenic magnetocaloric properties in heavy rare-earth based $HRENiGa_2$ (HRE = Dy, Ho, or Er) compounds. Sci China Mater, 2022, 66: 249

20 Zhang Y, Li S, Hu L, *et al.* Excellent magnetocaloric performance in the carbide compounds $RE_2Cr_2C_3$ (RE = Er, Ho, and Dy) and their composites. Mater Today Phys, 2022, 27: 100786

21 Li L, Yan M. Recent progress in the development of $RE_2TMTM'O_6$ double perovskite oxides for cryogenic magnetic refrigeration. J Mater Sci Tech, 2023, 136: 1–12

22 Xu P, Hu L, Zhang Z, *et al.* Electronic structure, magnetic properties and magnetocaloric performance in rare earths (RE) based RE_2BaZnO_5 (RE = Gd, Dy, Ho, and Er) compounds. Acta Mater, 2022, 236: 118114

23 Zhang Y, Tian Y, Zhang Z, *et al.* Magnetic properties and giant cryogenic magnetocaloric effect in B-site ordered antiferromagnetic Gd_2MgTiO_6 double perovskite oxide. Acta Mater, 2022, 226: 117669

24 Lionte S, Risser M, Muller C. A 15 kW magnetocaloric proof-of-concept unit: Initial development and first experimental results. Int J Refrigeration, 2021, 122: 256–265

25 Maiorino A, Mauro A, Del Duca MG, *et al.* Looking for energy losses of a rotary permanent magnet magnetic refrigerator to optimize its performances. Energies, 2019, 12: 4388

26 Shen J, Gao X, Li K, *et al.* Experimental research on a 4 K hybrid refrigerator combining GM gas refrigeration effect with magnetic refrigeration effect. Cryogenics, 2019, 99: 99–104

27 Law JY, Franco V, Moreno-Ramírez LM, *et al.* A quantitative criterion for determining the order of magnetic phase transitions using the magnetocaloric effect. Nat Commun, 2018, 9: 2680

28 Yakinthos JK. Crystal and magnetic structures of $TmFe_2Si_2$ and $TmNi_2Ge_2$ compounds. Influence of the d-metal charge on the anisotropy direction of the RT_2X_2 (R = rare earth, T = 3d or 4d metal and X = Si, Ge) compounds. J Magn Magn Mater, 1991, 99: 123–132

29 Moze O, Hofmann M, Buschow KHJ. Chromium sublattice magnetic ordering in a compound of the $ThCr_2Si_2$ type structure: $HoCr_2Si_2$. J Alloys Compd, 2000, 308: 60–63

30 Moze O, Rosenkranz S, Osborn R, *et al.* Magnetic excitations in tetragonal $HoCr_2Si_2$. J Appl Phys, 2000, 87: 6283–6285

31 Saensunon B, Stewart GA, Nishimura K. Crystal field interaction at the Tm^{3+} site in $TmCr_2Si_2$. J Alloys Compd, 2009, 476: 49–53

32 Janatová M, Vejpravová JP, Diviš M. Magnetic properties of RCr_2Si_2 compounds (R = Tb, Er). J Magn Magn Mater, 2010, 322: 1140–1142

33 Li L, Hu G, Umehara I, *et al.* Magnetic properties and magnetocaloric effect of $GdCr_2Si_2$ compound under hydrostatic pressure. J Alloys Compd, 2013, 575: 1–4

34 Moze O, Hofmann M, Cadogan JM, *et al.* Magnetic order in RCr_2Si_2 intermetallics. Eur Phys J B - Condensed Matter, 2003, 36: 511–518

35 Li L, Hutchison WD, Huo D, *et al.* Low-field giant reversible magnetocaloric effect in intermetallic compound $ErCr_2Si_2$. Scripta Mater, 2012, 67: 237–240

36 Toby BH. EXPGUI, a graphical user interface for GSAS. J Appl Crystlogr, 2001, 34: 210–213

37 Cui J, Huang Q, Toby BH. Magnetic structure refinement with neutron powder diffraction data using GSAS: A tutorial. Powder Diffr, 2012, 21: 71–79

38 Yang SX, Zheng XQ, Yang WY, *et al.* Tunable magnetic properties and magnetocaloric effect of TmGa by Ho substitution. Phys Rev B, 2020, 102: 174441

39 Green RW, Legvold S, Spedding FH. Magnetization and electrical resistivity of erbium single crystals. Phys Rev, 1961, 122: 827–830

40 Brommer PE. A generalization of the Inoue-Shimizu model. Physica B-Condensed Matter, 1989, 154: 197–202

41 Liu XB, Ryan DH, Altounian Z. The order of magnetic phase transition in $La(Fe_{1-x}Co_x)_{11.4}Si_{1.6}$ compounds. J Magn Magn Mater, 2004, 270: 305–311

42 Mo ZJ, Shen J, Yan LQ, *et al.* Low field induced giant magnetocaloric effect in TmGa compound. Appl Phys Lett, 2013, 103: 052409

43 Mo ZJ, Shen J, Yan LQ, *et al.* Low-field induced giant magnetocaloric effect in TmCuAl compound. Appl Phys Lett, 2013, 102: 192407

44 Li L, Yuan Y, Zhang Y, *et al.* Giant low field magnetocaloric effect and field-induced metamagnetic transition in TmZn. Appl Phys Lett, 2015, 107: 132401

45 Zhang Y, Wilde G. Magnetic properties and magnetocaloric effect in quaternary boroncarbides compound ErNiBC. Physica B-Condensed Matter, 2015, 472: 56–59

46 Li L, Saensunon B, Hutchison WD, *et al.* Magnetic properties and large reversible magnetocaloric effect in $TmMn_2Si_2$. J Alloys Compd, 2014, 582: 670–673

47 Zhang H, Xing C, Zhou H, *et al.* Giant anisotropic magnetocaloric effect by coherent orientation of crystallographic texture and rare-earth ion moments in HoNiSi ploycrystal. Acta Mater, 2020, 193: 210–220

48 Bebenin NG, Zainullina RI, Ustinov VV, *et al.* Magnetic properties of $La_{0.7-x}Pr_xCa_{0.3}MnO_3$ single crystals: When is Banerjee criterion applicable? J Magn Magn Mater, 2014, 354: 76–80

49 Franco V, Conde A, Pecharsky VK, *et al.* Field dependence of the magnetocaloric effect in Gd and $(Er_{1-x}Dy_x)Al_2$: Does a universal curve exist? Europhys Lett, 2007, 47: 47009

50 Oesterreicher H, Parker FT. Magnetic cooling near curie temperatures above 300 K. J Appl Phys, 1984, 55: 4334–4338

Author contributions   Zheng X designed the idea of this research. Xi L, Liu C, Wang D, Xu J, Yang S, Gao Y and Jin B performed the experiments including sample synthesis, magnetic measurements and XRD analysis. Xu J and Yin W performed the NPD experiments. Zhu M and Xu W performed the TEM experiments. Zheng X performed the data analysis and prepared the original manuscript. All the other authors contributed to the discussion.

Conflict of interest   The authors declare that they have no conflict of interest.

Lei Xi graduated from the School of Materials Science and Engneering, University of Science and Technoloy Beijing (USTB), and currently he is a PhD student at the School of Materials Science and Engineering, Anhui University (AHU). His research interests focus on magnetic properties and the magnetocaloric effect of rare-earth-based compounds.

Xinqi Zheng recieved his PhD degree from the Institute of Physics, Chinese Academy of Sciences. During his PhD study, he carried out research on neutron powder diffraction of magnetic materials as a guest researcher. Currently, he is an associate professor at the School of Materials Science and Engineering, USTB. His research interest focuses on rare-earth-based low-temperature magnetic refrigerant materials and abnormal magnetic thermal expansion materials.

Er-Y-Cr-Si化合物在极低温区的巨低场磁热效应

奚磊[1,2]，郑新奇[1*]，高亚伟[1]，许家旺[3,4]，刘超凡[1]，王鼎淞[1]，徐菊萍[5,6]，殷雯[5,6]，杨淑娴[1,3]，靳宝杰[1]，朱梦媛[1]，许玮峯[1]，申见昕[1]，张静言[1]，黄河[1]，吴燕飞[1]，顾飞[1]，史慧宇[1]，陶怡璇[1]，王守国[1,2*]，沈保根[3,7]

摘要　高性能低温低场磁热材料在气体液化等领域具有重要的应用前景. 本团队通过真空电弧熔炼的方式成功合成了一系列多晶 $Er_{1-x}Y_xCr_2Si_2$ ($0 \leqslant x \leqslant 0.8$)样品，这些材料表现出巨大的低场磁热效应. 其中Cr含量为0.1的样品显示出最好的低场磁热性能以及接近2 K的合适的工作温区. 更重要的是，在0–1 T的磁场变化下，该样品的最大磁熵变峰值以及最大绝热温变峰值分别高达19.2 J kg^{-1} K^{-1}和4.3 K. 其磁熵变峰值为目前已报道的20 K以下温区合金类磁热材料的最大值. 通过Arrott曲线，平均场理论以及约化磁熵变曲线等手段，证明了磁相变特征为二级相变. 物理机理分析表明，10%的Y替代导致高达15.9%的磁熵变峰值增强的原因在于替代样品所具有的大饱和磁化强度以及小饱和磁场.